Novel two-dimensional AlSb and InSb monolayers with a double-layer honeycomb structure : a first-principles study

ROYAL SOCIETY OF CHEMISTRY

ARTICLE TYPE

Cite this: DOI: 10.1039/xxxxxxxxxx

Novel two-dimensional of AlSb and InSb monolayers with double-layer honeycomb structure: A First-principle study

A. Bafekry[1†], M. Faraji[3], M. M. Fadlallah[4], H. R. Jappor[5], S. Karbasizadeh[6], M. Ghergherehchi[7], I. Abdolhosseini Sarsari[6], A. Abdolahzadeh Ziabari[8],

Received Date
Accepted Date

DOI: 10.1039/xxxxxxxxxx

www.rsc.org/journalname

In this work, motivated by the fabrication of AlSb monolayer, we have only focused on the electronic, mechanical, and optical properties of AlSb and InSb monolayers with double-layer honeycomb structure employing the density functional approach. The phonon band structure and cohesive energy confirm the stability of XSb (X=Al and In) monolayers. The mechanical properties reveal XSb monolayers have brittle nature. Using the GGA+SOC (HSE+SOC) functional bandgap of AlSb monolayer is predicted to be direct, while InSb has a metallic character using both functionals. We find that XSb (X=Al, In) two-dimensional bodies can absorb the ultraviolet. The present findings suggest several applications of AlSb and InSb monolayers in novel optical and electronic usages.

Graphene, as the first two-dimensional (2D) material to be exfoliated in experiment[1] has sparked tremendous curiosity due to its exceptional properties. Graphene breaks down the ingrained realization that 2D cannot exist statically and fosters a new field of research on the nanoscale. This 2D material is an excellent choice for use in lithium-ion batteries[2],nanosensors[3], and nanoelectronics applications[4]. Its high charge carrier mobility shows a graphene's semi-metallic behavior, as shown by the linear dispersion at the Dirac point[5,6]. However, the lack of bandgap energy is a barrier to the direct incorporation of graphene into some electronic equipment, particularly in photovoltaic cells. Its electronic properties must be adjusted To allow graphene functionally feasible with high performance in electronic devices. Then, countless types of 2D material like graphene structures have been peeled off in single layers and using various exfoliation methods. The unconventional electronic properties of some 2D material structures such as silicene[7], phosphorene[8], tinene[9], antimonene[10], and germanene[11] have increasingly aroused the interest of researchers.

The III-V binary compound monolayers are among the well-known compounds that have been investigated their properties extensively. The 2D III-V materials are composed of two groups located beside the IV group in the periodic table. In general, it has been found that the electronic properties of these 2D compounds, especially the energy gap, are primarily divided into three types[12]. The first type being materials with a very narrow bandgap that can be promising materials in infrared detectors, low-power nanoelectronics, and Schottky diodes[13,14]. The second type is the 2D materials with an energy gap greater than 2 eV, and the third type is the materials that have a wide energy gap with weak electrical conductivity, such as GaP, InN, and GaN And AlN[15,16].

Although some of these monolayers are similar in geometric structures to the 2D group-IV materials, their characteristics are far from it. For example, the energy gap of hexagonal boron nitride (hBN) is approximately equal to 4.64 eV, although this 2D monolayer is similar to graphene as it has a planar structure[17]. However, antimony-based monolayers have gained much interest over the last few decades because of their particular purposes. Among them, 2D aluminum antimonide (AlSb) has been investigated in theoretical and experimental calculations due to its esoteric performance[18,19]. Furthermore, AlSb is of significant technological, and scientific importance with an indirect gap of 1.62eV and distinctive band alignment[20]. It can be used in a wide variety of applications such as sodium-ion, and lithium-ion

[1] *Department of Radiation Application, Shahid Beheshti University, 19839 69411 Tehran, Iran.*
[2] *Department of Physics, University of Antwerp, Groenenborgerlaan 171, B-2020 Antwerp, Belgium.*
[3] *TOBB University of Economics and Technology, Sogutozu Caddesi No 43 Sogutozu, 06560, Ankara, Turkey.*
[4] *Department of Physics, Faculty of Science, Benha University, 13518 Benha, Egypt.*
[5] *Department of Physics, College of Education for Pure Sciences, University of Babylon, Hilla, Iraq.*
[6] *Department of Physics, Isfahan University of Technology, Isfahan, 84156-83111, Iran.*
[7] *Department of Electrical and Computer Engineering, Sungkyunkwan University, 16419 Suwon, Korea.*
[8] *Nano Research Lab, Lahijan Branch, Islamic Azad University, Lahijan, Iran.*
† *To whom correspondence should be addressed. Email: bafekry.asad@gmail.com*

storage[21], high-speed electronic devices, hybrid Hall effect devices[22], tunneling field-effect transistors[23], and as a buffer layer material in promoting the growth of the GaSb film[24,25]. Experiments demonstrate that the growth of the AlSb layer can perform on the Si-(111) substrate by molecular beam epitaxy (MBE)[26].

Very recently, following theoretical prediction, Qin et al. manifested that AlSb monolayers can be produced epitaxially on graphene-covered SiC-(0001) utilizing MBE[27]. Also, it is discovered that the AlSb monolayer is more stable than its bulk zinc-blende (ZB) structures and has an energy gap of 0.93 eV, which is less than that of bulk 1.6 eV. Indium antimonide (InSb), another antimony-based monolayer material, has also been synthesized and characterized by MBE[28]. Besides, Jia et al.[29] documented the fabrication of InSb on the Si-(100) substrate utilizing GaSb and AlSb buffers with high responsivity. On the other hand, it was found that InSb possesses unusual properties such as small electron effective mass, high charge density, robust spin-orbit interaction, and outstanding carrier mobility[30,32,33]. Also, it has been predicted that the free-standing InSb is a stable semiconductor with a bandgap of 0.69 eV[34] and ZB single crystals. All the studies suggest that InSb will be an essential 2D semiconductor material in optoelectronics, low-power electronics, photonic devices, and future applications[35–37].

The present paper aims to validate the structural, electronic, mechanical, and optical properties of AlSb and InSb monolayers in the double-layer honeycomb structure with employing density functional theory (DFT). It has not yet been established the structural, mechanical, electronic, and optical properties of AlSb and InSb monolayers. Thus, we will try to fill some of the deficiencies in the above properties of AlSb and InSb monolayers. The current results represent a significant step forward in our understanding of the properties AlSb and InSb monolayers, which structural and chemical alterations can tune. Our results provide insight into the new family of these 2D materials monolayers and could advance and encourage experiments in producing these monolayers for innovative nanodevices and applications.

1 Method

The DFT approach in this work was carried with applying the plane-wave basis projector augmented wave (PAW) method together with Perdew-Burke-Ernzerhof(PBE)[38,39] functional as available in the Vienna *ab-initio* Simulation Package (VASP)[40,41]. Moreover, Heyd-Scuseria-Ernzerhof (HSE06)[42] functional employed for more precise bandgap value. The kinetic energy cut-off of 500 eV was adjusted for plane-wave expansion, and the energy was converged until variation in the energies falls below 10^{-8} eV. Optimizing structures, total Hellmann-Feynman forces were reduced to 10^{-7} eV/Å. $21\times21\times1$ Γ centered k-point grid was used for the primitive unit cells by using Monkhorst-Pack[43]. The XSb (X=Al, In) monolayers were modeled with a vacuum region more than 20 Å to avoid interaction between neighboring monolayers. Charge transfers analysis is accomplished using the Bader technique[44]. Here, the Van der Waals (vdW) correction proposed to describe the long-range vdW interactions[45]. The phonon characteristics were gained from the small displacement method as implemented in the PHONOPY code[46]. The thermal stability is also examined by conducting the AIMD simulations at 400K. The training set is prepared by conducting ab-initio molecular dynamics (AIMD) simulations over $3\times3\times1$ supercells with $7\times7\times1$ k-point grids.

2 Structural properties

The top and side views of atomic structures of AlSb and InSb monolayers in the double-layer honeycomb structure are shown in Figs. 1(a,b). In these monolayers, a graphene-like honeycomb lattice with a hexagonal primitive cell includes four atoms, and a primitive cell is revealed as a red parallelogram. The unit-cell lattice constants for the AlSb and the InSb monolayers are determined to 4.24 Å and 4.35 Å, respectively. We find that the bond lengths d_1 (d_2) of the AlSb and InSb are 2.68 Å (2.8 6Å) and 2.86Å (3.23 Å) respectively, while the bond angles θ_1 and θ_2 are 104.23° and 114.31°, respectively. Notice that the studied monolayers are not planar lattice, and thickness of considered structures are calculated 3.96 Å and 4.33 Å for the AlSb and InSb, respectively. Both structures have a spacegroup of P3m1 without inversion symmetry (number 156, extended Bravais lattice symbol of hP2). The structural parameters are given in Table I.

The cohesive energy per atom was calculated as following

$$E_{coh} = \frac{E_{tot} - 2E_X - 2E_{Sb}}{4}, \quad (1)$$

where E_X and E_{Sb} represent the energies of isolated single X(Al,In) and Sb atoms, respectively; 4 is the total number of atoms in the unit cell, and E_{tot} represents the total energy of the XSb monolayers. The cohesive energy of AlSb and InSb monolayers are realized to be -5.04 and -6.43 eV/atom, respectively. The negative cohesive energy for these layers implies that the free-standing nanostructures are likely to be stable. The more negative values for cohesive energies suggest that the energetically more stable monolayer. The structures demonstrate more stability for a small atomic mass and atomic radius and high electronegativity. We found out that the electrostatic potential of surveyed monolayers is flat in the vacuum region. The work function was calculated using the following $\Phi = E_{vacuum} - E_F$, where E_{vacuum} is the energy of the vacuum energy, which is calculated from the electrostatic potential of the monolayers, and E_F is the Fermi energy. The calculated work function for the AlSb and InSb monolayers are 4.41 and 4.45 eV, respectively, which reduces as the electronegativity of the X atom decreases.

The dynamical stability of XSb monolayers is approved by calculating their phonon spectra through the whole Brillouin Zone (BZ) as presented in Fig. 1(b). No imaginary vibration can be found in the first BZ for studied monolayers, indicating its dynamical stability. The different atomic masses of Al/In and Sb atoms lead to a bandgap in the phonon bands in the interval from approximately 135 cm^{-1} to 220 cm^{-1} for AlSb and from 95 cm^{-1} to 115 cm^{-1} for InSb. Due to the atomic mass, In is larger than Al's, the phonon bandgap of InSb is smaller than that of AlSb. Note the opening up of the gap in the case of AlSb and InSb due to the large mass difference in the chemical species present, Sb and Al/In. Therefore the phonon dispersion results suggest that 2D graphene-like XSb structures are

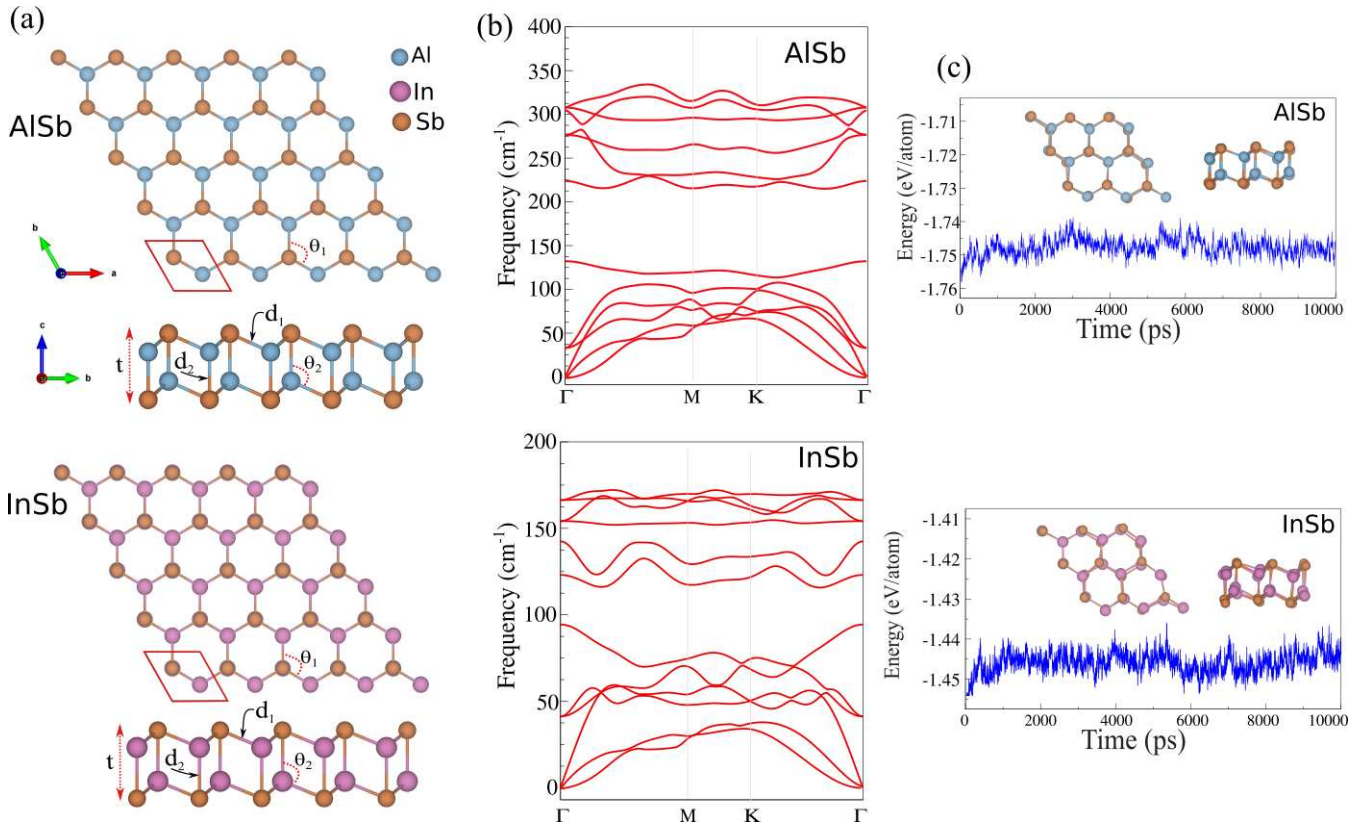

Fig. 1 (a) Atomic structures and (b) phonon band dispersion of the AlSb and InSb monolayers, respectively. The primitive unit cell indicated by a red parallelogram. (c) Ab initio molecular dynamics (AIMD) at 400 K. The optimized structures are indicated in the same panel.

Table 1 Structural and electronic parameters of AlSb and InSb monolayers, as shown in Fig. 1, including lattice constant *a*; bond length between atoms d_1 (d_2); bond angles between atoms θ_1 (θ_2); thickness defined by the difference between the largest and smallest z coordinates (t); cohesive energy per atom, (E_{coh}); charge transfer ΔQ; work function Φ; bandgap E_g with Pbe (Pbe+SOC,HSE,HSE+SOC) ; shear modulus (S); Young's modulus (Y); and Poisson's ratio (ν), respectively.

Sys.	a (Å)	$d_{1,2}$ (Å)	$\theta_{1,2}$ (°)	t (Å)	E_{coh} (eV/atom)	ΔQ (e)	Φ (eV)	E_g (eV)	S GPa	Y GPa	ν
AlSb	4.24	2.68 (2.86)	104.23 (114.31)	3.96	-5.04	1.45	4.14	0.3 (0.08, 0.90, 0.70)	6.00	14.82	0.23
InSb	4.35	2.86 (3.23)	106.36 (112.41)	4.33	-6.43	0.34	4.45	M (0.10, 0.06, 0.09)	3.96	9.94	0.25

dynamically stable. Phonon spectra calculations reveal the dynamical stability of the pristine AlSb and InSb monolayers. Apart from the three acoustical phonon branches, there are nine optical phonon branches. Among the nine optical phonon modes, there are two doubly-degenerate phonon mode below 50 cm^{-1} which represents the shear vibration of the sub-XSb layers concerning each other. On the other hand, the phonon mode around 100-150 cm^{-1} shows the breathing-like vibration of the XSb sublayers. Note that the frequency of such phonon mode is higher in these monolayers since the sub-XSb layers are chemically bonded in contrast to usual vdW layered materials. In addition, in the case of AlSb monolayer, there are two non-degenerate and four doubly-degenerate phonon branches whose frequencies reside between 200-350 cm^{-1} while in the case of InSb the frequencies are lower (125-175 cm^{-1}). This is directly related to the stronger chemical bonding between Al-Sb as compared to In-Sb.

Additionally, the thermal stability of AlSb and InSb monolayers are further examined by ab initio molecular dynamics simulations (AIMD) using a $3 \times 3 \times 1$ supercell at 400 K. AIMD simulation for both monolayers at 400 K is shown in Fig. 1(c), where the optimized structures are indicated in the inset. The thermal dynamic investigations are started with the optimized structures at 0 K. The temperature was increased to 400 K. As can be noticed from the snapshots, apart from minor distortions, the crystal structures of AlSb and InSb monolayers are preserved, further confirming the stability even at least up to 400 K.

Turning to the mechanical stability of XSb monolayers, the linear-elastic properties of 2D materials can be directly examined by calculating the elastic tensor elements applying the harmonic approximation. The linear elastic coefficients, C_{ij}, the mechanical stability of both structures are endorsed. The elastic coefficients should obey the Born criteria: $C_{11} - C_{12} > 0$, $C_{44} > 0$, and $C_{1x}^2 < 0.5 * C_{xx}(C_{11} + C_{12})$ $(x = 3,4)$ which are satisfied for both monolayer. The elastic constants are $C_{11} = 32.303$ (22.453)

GPa, C_{12} = 9.380 (7.746) GPa, C_{13} = 0.001 (0.031) GPa, C_{14} = 0.00 (0.00) GPa and C_{44} = 11.462 (7.354) GPa for AlSb (InSb) monolayer. The elastic constants and Young's modulus of AlSb, 14.82, GPa, are larger than that of the InSb monolayer, 9.94 GPa, because the size of AlSb is smaller the InSb monolayer. It is found experimentally, the elastic constants and Young's modulus increase as the size of nanostructure decrease[47,48]. Therefore the AlSb has higher stiffness (hardness) than the InSb monolayer. The shear modulus calculation confirms that the ability of AlSb monolayer (6.00 GPa) to resist the deformation under stress is more than InSb (3.96 GPa). The value of Poisson's ratio is 0.23, and 0.25 for AlSb and InSb, respectively, which indicates XSb has a brittle behavior (less than 0.33[49]).

We determine the lowest energy stacking configuration of AlSb and InSb bilayers, including structural optimization. The different stacking patterns, including AA_1, AA_2, AB_1, and AB_2 that we considered, are shown in Fig. S1(a) of the supplementary information. Side views of the stacking structures are shown in the inset. Our results show that the most stable stacking is AB_2 for both XSb bilayers. Then the binding energy is calculated to see where the bilayers are most stable in terms of the interlayer distance. This is done through the formula below: $E_b = E_{2L-XSb} - 2E_{XSb}$ In the recipe above, E_{2L-XSb} represents the energy of the XSb bilayers, while E_{XSb} gives the energy of each XSb layer individually. This energy is determined relative to the interlayer distance for AlSb bilayer in Fig. S1(b), where the most stable interlayer distance between the two Sb atoms, the lowest Sb in the layer above, and the highest Sb in the layer below is determined to be 2.99 Å. Binding energy is also determined for the InSb bilayer in Fig. S1(c) for different amounts of interlayer distance. The inset shows which atoms are included in the calculation of the distance between the layers. The two Sb atoms involved in this calculation are the same Sb atoms as the ones in the AlSb bilayer.

3 Electronic properties

The electronic band structure with the corresponding density of states (DOS) and partial DOS (PDOS) of XSb monolayers are depicted in Figs. 2(a,b) and Fig. S2. Our results show that AlSb is the direct semiconductor with the bandgap of 0.08 eV at the Γ point within PBE functional plus SOC (PBE+SOC). The HSE results are consistent with PBE for the type of the direct semiconducting bandgap, although HSE was conducted with the addition of SOC. Based on the acquired band structure by the HSE (HSE+SOC) method, the direct bandgap of AlSb was estimated to be 0.90 (0.70) eV. To explain the origin of the electronic states, the DOS/PDOS is shown in Figs. 2(a,b). From DOS and PDOS, the VBM is composed of the Sb-$p_{x,y}$, while the CBM comes from Al-s orbital states. Unlike AlSb, the InSb monolayer exhibits metallic characteristics in PBE functional. PBE+SOC, HSE, and HSE+SOC functionals, though applied, give a very small bandgap of 0.10, 0.06, and 0.09 eV, respectively, rendering InSb a semiconductor. The CBM and VBM of this band structure are both located at Γ point except for PBE+SOC. we found band inversion among states of the same parity in PBE+SOC calculation. It appears that SOC is the deciding factor here for the observed topological properties, while in HSE+SOC calculation the SOC is not a deciding

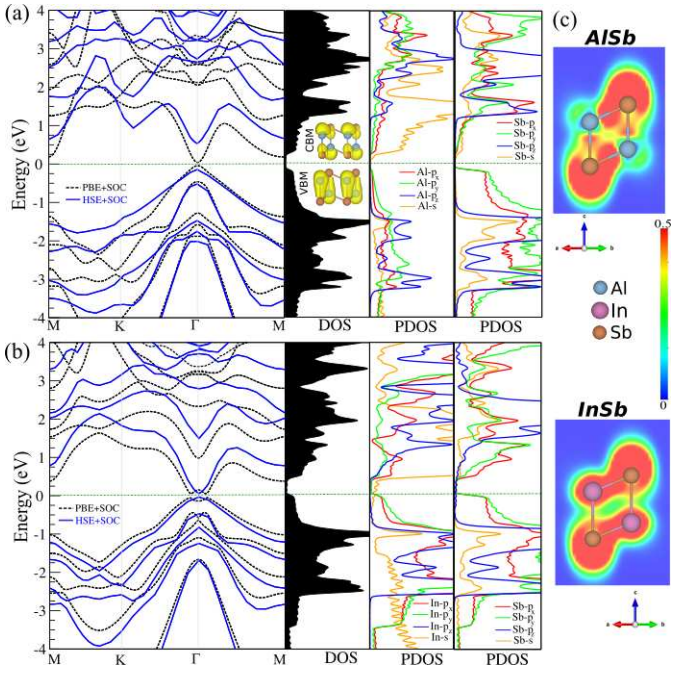

Fig. 2 Electronic band structure with the corresponding DOS and PDOS of (a) AlSb and (d) InSb monolayers. Charge densities of the valance band maximum (VBM) and conduction band minimum (CBM) orbitals of AlSb indicated as inset. (c) Electron localization function (ELF) maps. The zero of energy is set to Fermi-level.

factor. The exact impact of SOC on topological properties deserve to study in future studies. Energy bands near the Fermi energy are shaped mainly by s and $p_{x,y}$ orbital states. We found that the metallic character of InSb (PBE) originates from Sb-$p_{x,y}$ and In-s orbitals.

The electron localization function (ELF) of XSb monolayers along with the (001) plane is illustrated in Fig. 2(c), where the color red indicates intense localization while blue gives the lowest amount of intensity. The color graph is shown in this same part of the figure, where the number 0.5 belongs to the color red as maximum localization and 0.0 goes to the other end of the spectrum with the color blue. For AlSb, the ELF surrounding the Sb atoms are portrayed with the color red and as the bond approaches the atoms of Al, there is a sudden change of localization. For the monolayer of InSb, however, two of the four bonds connecting In and Sb are much stronger than the other two. This can be inferred as the localization between these bonds reaches the maximum amount and gives the color red in the ELF map. Al and In atoms are positively charged, and besieged by Sb atoms are negatively charged. We know that the charge redistribution stem from the different electronegativity of Al (1.6), In (1.8), and Sb (2.1). Based on Bader charge analysis, we found that each Sb atom gains about 1.45e and 0.34e from the nearby Al and In atoms in AlSb and InSb, respectively.

4 Optical features

The real and imaginary dielectric functions are calculated to inquire about the optical features of AlSb and InSb monolayers, as shown in Fig. 3 which are applied to describe the interaction be-

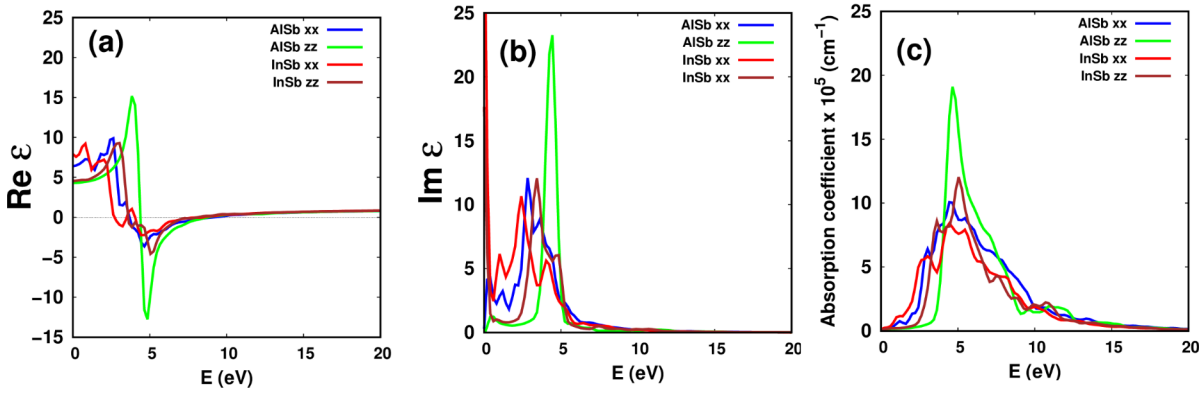

Fig. 3 (a) Real (Re(ε)), (b) and imaginary parts of the dielectric function (im(ε)), and (c) absorption coefficient vs. photon incident energy for the AlSb and InSb monolayers

tween the electromagnetic field and the monolayers. This interaction depends on the electronic band structure of the monolayers. The Kramers-Kronig relations connect the real and imaginary parts of the dielectric constants. The absorption or reflection occurs when the dielectric function is negative. The dielectric function has two interband transitions, and the absorption edges excitation and plasmon excitation. The absorption coefficient ($\alpha(\omega)$) can be expressed as follows:

$$\alpha(\omega) = \sqrt{2}\omega\sqrt{\sqrt{\varepsilon_1^2(\omega)+\varepsilon_2^2(\omega)}-\varepsilon_1(\omega)}, \tag{2}$$

where $\varepsilon_1(\omega)$ and $\varepsilon_2(\omega)$ are considered as the real and imaginary terms of the dielectric function at angular frequency ω, respectively, and they are evaluated using:

$$\varepsilon_2(\omega) = \frac{(2\pi e)^2}{(m\omega)^2 V}\sum_{k,i}\langle\psi_k^v|p_i|\psi_k^c\rangle\delta(E_{\psi_k^c}-E_{\psi_k^v}-\hbar\omega), \tag{3}$$

and also the Kramers-Kronig relation is utilized to gain

$$\varepsilon_1(\omega) = \frac{2}{\pi}P\int d\omega' \frac{\varepsilon_2(\omega')}{\omega'-\omega}, \tag{4}$$

where m, e, p and V imply mass, the charge of the electron, momentum operator, and the volume of the supercell, respectively. The wavefunctions ψ_k^v, and ψ_k^c represent the valence band and conduction band states, respectively. The eigenvalues $E_{\psi_k^v}$ and $E_{\psi_k^c}$ refer to the energy of the occupied and unoccupied valence and conduction band states, respectively, and $\hbar\omega$ indicates the incident light energy.

In Fig. 3(a), the static value of the real part of the dielectric is 6.44 and 4.32 for AlSb monolayer, and 8.10 and 4.56 for InSb monolayer in xx and zz directions, respectively. Due to the structure's symmetry, the yy direction's value is the same as in xx direction. Many peaks in xx direction appear from 0.5 eV to 5.0 eV for both monolayers. While in zz direction, a distinct peak appears at 3.91 eV for AlSb and 3.17 eV for InSb (Fig. 3b). For the imaginary part of the dielectric function (Fig. 3(b)), it can be seen that the imaginary part value in xx direction tends to be positive infinite for InSb, which indicates the highly intense metallic behavior. At the same time, it is tiny for AlSb due to its semiconducting character. There are many peaks in the energy range 0.5 eV to 5.0 eV for both monolayers in xx direction (similar to the real part). For zz direction, as in the real part, there is a distinct peak at 4.41 eV for AlSb monolayer and 3.53 eV for InSb monolayer. The optical absorption is related to the imaginary part of the dielectric function where the electrons in occupied states are induced by absorbing a photon into unoccupied states. The prominent absorption peak appears around 5 eV in all directions, which means the AlSb and InSb are more active in the ultraviolet region. Also, we found a peak around 2.5 eV for xx component for AlSb monolayer and for xx and zz components for InSb, which means these monolayers can absorb visible light. Furthermore, a minimal peak for xx component at 0.75 eV for both monolayers means a possibility of the interaction between the infrared spectrum with the materials. The absorption spectra of AlSb monolayer are slightly shifted towards the high energy compared to the corresponding spectrum of InSb monolayer due to the semiconducting and metallic character of AlSb and InSb, respectively.

5 Conclusion

To sum up, motivated by the fabrication of the AlSb monolayer in the double-layer honeycomb structure, we surveyed the electronic and optical properties of AlSb and InSb monolayers using density functional calculations. The stability of XSb (X=Al and In) monolayers have been confirmed by phonon spectra and cohesive energy. The elastic constants, C_{11} = 32.303 (22.453) GPa, C_{12} = 9.380 (7.746) GPa, C_{13} = 0.001 (0.031) GPa, C_{14} = 0.00 (0.00) GPa, and C_{44} = 11.462 (7.354) GPa, for AlSb (InSb) monolayer satisfy Born criteria, while the Young's modulus of AlSb monolayer, 14.82, GPa, are larger than that of the InSb monolayer, 9.94 GPa. The XSb monolayers are brittle, and the AlSb monolayer has a higher hardness factor than the InSb monolayer. The AlSb electronic structure study revealed that the VBM and CBM is composed of the Sb-$p_{x,y}$ and Al-s orbital states, respectively. The AlSb is a semiconductor with a bandgap of 0.3 (0.7) eV using PBE+SOC (HSE+SOC) method, which is fascinating for nanoelectronics applications. The InSb monolayer shows a band structure with metallic characteristics in PBE+SOC. While considering HSE functional, InSb is a semiconductor with a small bandgap 0.06 eV. The optical properties showed that the XSb monolay-

ers could be active materials in the ultraviolet region due to the prominent absorption peak around 5 eV. These observations have many implications for research into the application of XSb monolayers in novel electronic and optical systems.

6 Declaration of competing interest

The authors declare that they have no known competing financial interests or personal relationships that could have appeaf to influence the work reported in this paper.

7 ACKNOWLEDGMENTS

This work was supported by the National Research Foundation of Korea (NRF) grant funded by the Korea government (MSIT) (NRF-2015M2B2A4033123).

References

1 K.S. Novoselov, A.K. Geim, S. V. Morozov, D.A. Jiang, Y.Y. Zhang, S. V. Dubonos, A.A. Firsov, I. V. Grigorieva, A.A. Firsov, Electric Field Effect in Atomically Thin Carbon Films, Sci. 306 (2004) 666-669.

2 Y. Jing, Graphene, inorganic graphene analogs and their composites for lithium ion batteries, J. Mater. Chem A. 2 (2014).

3 G.S. Kulkarni, K. Reddy, Z. Zhong, X. Fan, Graphene nanoelectronic heterodyne sensor for rapid and sensitive vapour detection, Nat. Commun. 5 (2014) 1-7.

4 F. Xia, T. Mueller, Y.M. Lin, A. Valdes-Garcia, P. Avouris, Ultrafast graphene photodetector, Nat. Nanotechnol. 4 (2009) 839-843.

5 S. V. Dubonos, I. V. Grigorieva, K.S. Novoselov, S. V. Morozov, A.A. Firsov, A.K. Geim, M.I. Katsnelson, D. Jiang, S. V. Morozov, D. Jiang, M.I. Katsnelson, I. V. Grigorieva, S. V. Dubonos, A.A. Firsov, Two-dimensional gas of massless Dirac fermions in graphene, Nat. 438 (2005) 197-200.

6 K.S. Novoselov, Z. Jiang, Y. Zhang, S. V. Morozov, H.L. Stormer, U. Zeitler, J.C. Maan, G.S. Boebinger, P. Kim, A.K. Geim, Room-Temperature Quantum Hall Effect in Graphene, Sci. 315 (2007) 1379-1379.

7 W. Wei, Y. Dai, B. Huang, T. Jacob, Many-body effects in silicene, silicane, germanene and germanane, Phys. Chem. Chem. Phys. 15 (2013) 8789-8794.

8 H. Liu, A.T. Neal, Z. Zhu, D. Tomanek, P.D. Ye, Phosphorene: A New 2D Material with High Carrier Mobility, ACS Nano. 8 (2014) 4033-4041.

9 L. Matthes, O. Pulci, F. Bechstedt, Optical properties of two-dimensional honeycomb crystals graphene, silicene, germanene, and tinene from first principles, New J. Phys. 16 (2014) 105007.

10 T. Lei, C. Liu, J.L. Zhao, J.M. Li, Y.P. Li, J.O. Wang, R. Wu, H.J. Qian, H.Q. Wang, K. Ibrahim, Electronic structure of antimonene grown on Sb_2Te_3 (111) and Bi_2Te_3 substrates, J. Appl. Phys. 119 (2016) 015302.

11 Z. Ni, E. Minamitani, Y. Ando, S. Watanabe, Germanene and stanene on two-dimensional substrates: Dirac cone and Z2 invariant, Phys. Rev. B. 96 (2017) 075427.

12 C.S. Liu, Z.W. Teng, X.J. Ye, X.H. Yan, Two-dimensional tetragonal AlP monolayer: Strain-tunable direct-indirect band-gap and semiconductor-metal transitions, J. Mater. Chem. C. 5 (2017) 5999-6004.

13 L.E. Wernersson, Narrow gap nanowires: From nanotechnology to RF-circuits on Si, J. Appl. Phys. 2015, 112810.

14 D.L. Rode, Electron transport in InSb, InAs, and InP, Phys. Rev. B. 3 (1971) 3287-3299.

15 H. Sahin, S. Cahangirov, M. Topsakal, E. Bekaroglu, E. Akturk, R.T. Senger, S. Ciraci, Monolayer honeycomb structures of group-IV elements and III-V binary compounds: First-principles calculations, Phys. Rev. B. 80 (2009) 155453.

16 H.L. Zhuang, A.K. Singh, R.G. Hennig, Computational discovery of single-layer III-V materials, Phys. Rev. B - Condens. Matter Mater. Phys. 87 (2013) 165415.

17 M. Topsakal, E. Akturk, S. Ciraci, First-principles study of two- and one-dimensional honeycomb structures of boron nitride, Phys. Rev. B 79 (2009) 115442.

18 M.C. Lucking, W. Xie, D.H. Choe, D. West, T.M. Lu, S.B. Zhang, Traditional Semiconductors in the Two-Dimensional Limit, Phys. Rev. Lett. 120 (2018) 086101.

19 I. Lucci, S. Charbonnier, L. Pedesseau, M. Vallet, L. Cerutti, J.B. Rodriguez, E. Tournie, R. Bernard, A. Letoublon, N. Bertru, A. Le Corre, S. Rennesson, F. Semond, G. Patriarche, L. Largeau, P. Turban, A. Ponchet, C. Cornet, Universal description of III-V/Si epitaxial growth processes, Phys. Rev. Mater. 2 (2018) 060401.

20 D.M. Triches, S.M. Souza, C.M. Poffo, J.C. De Lima, T.A. Grandi, R.S. De Biasi, Structural instability and photoacoustic study of AlSb prepared by mechanical alloying, J. Alloys Compd. 505 (2010) 762-767.

21 S.Y. Son, D. Lee, J. Hur, I.T. Kim, Facile synthesis of aluminum-antimony alloys and their application for lithium-ion and sodium-ion storage, Nanotechnol. 17 (2017) 7575-7578.

22 M. Johnson, B.R. Bennett, M.J. Yang, M.M. Miller, B. V. Shanabrook, Hybrid Hall effect device, Appl. Phys. Lett. 71 (1997) 974-976.

23 Y. Zeng, C.I. Kuo, R. Kapadia, C.Y. Hsu, A. Javey, C. Hu, Two-dimensional to three-dimensional tunneling in InAs/AlSb/GaSb quantum well heterojunctions, J. Appl. Phys. 2013, 024502.

24 S.H. Vajargah, M. Couillard, K. Cui, S.G. Tavakoli, B. Robinson, R.N. Kleiman, J.S. Preston, G.A. Botton, Strain relief and AlSb buffer layer morphology in GaSb heteroepitaxial films grown on Si as revealed by high-angle annular dark-field scanning transmission electron microscopy, Appl. Phys. Lett. 98 (2011) 082113.

25 Y. Wang, P. Ruterana, L. Desplanque, S. El Kazzi, X. Wallart, Strain relief at the GaSb/GaAs interface versus substrate surface treatment and AlSb interlayers thickness, J. Appl. Phys. 109 (2011) 023509.

26 A. Proessdorf, M. Hanke, B. Jenichen, W. Braun, H. Riechert, Volmer-Weber growth of AlSb on Si(111), Appl. Phys. Lett.

102 (2013) 041601.

27 L. Qin, Z.H. Zhang, Z. Jiang, K. Fan, W.H. Zhang, Q.Y. Tang, H.N. Xia, F. Meng, Q. Zhang, L. Gu, D. West, S. Zhang, Y.S. Fu, Realization of AlSb in the Double-Layer Honeycomb Structure: A Robust Class of Two-Dimensional Material, ACS Nano. (2021).

28 D. Pan, D.X. Fan, N. Kang, J.H. Zhi, X.Z. Yu, H.Q. Xu, J.H. Zhao, Free-Standing Two-Dimensional Single-Crystalline InSb monolayers, Nano Lett. 16 (2016) 834-841.

29 B.W. Jia, K.H. Tan, W.K. Loke, S. Wicaksono, S.F. Yoon, Growth and characterization of InSb on (1 0 0) Si for mid-infrared application, Appl. Surf. Sci. 440 (2018) 939-945.

30 P. Caroff, J.B. Wagner, K.A. Dick, H.A. Nilsson, M. Jeppsson, K. Deppert, L. Samuelson, L.R. Wallenberg, L. Wernersson, High-Quality InAs/InSb Nanowire Heterostructures Grown by Metal-Organic VaporâĂŘPhase Epitaxy, Small. 4 (2008) 878-882.

31 O. Gul, D.J. Van Woerkom, I. Van Weperen, D. Car, S.R. Plissard, E.P.A.M. Bakkers, L.P. Kouwenhoven, Towards high mobility InSb nanowire devices, Nanotechnol. 26 (2015) 215202.

32 I. Vurgaftman, J.R. Meyer, L.R. Ram-Mohan, Band parameters for III-V compound semiconductors and their alloys, J. Appl. Phys. 89 (2001) 5815-5875.

33 A.A. Khan, M. Herrera, N. FernÃąndez-Delgado, D.F. Reyes, J. Pizarro, E. Repiso, A. Krier, S.I. Molina, Investigation on Sb distribution for InSb/InAs sub-monolayer heterostructure using TEM techniques, Nanotechnol. 31 (2020) 025706.

34 D. Di Sante, A. Stroppa, P. Barone, M.H. Whangbo, S. Picozzi, Emergence of ferroelectricity and spin-valley properties in two-dimensional honeycomb binary compounds, Phys. Rev. B 91 (2015) 161401.

35 Z. Wang, F. Sun, J. Liu, Y. Tian, Z. Zhang, Y. Zhang, X. Wei, T. Guo, J. Fan, L. Ni, L. Duan, Electric field and uniaxial strain tunable electronic properties of the InSb/InSe heterostructure, Phys. Chem. Chem. Phys. 22 (2020) 20712-20720.

36 M. De La Mata, R. Leturcq, S.R. Plissard, C. Rolland, C. Magen, J. Arbiol, P. Caroff, Twin-Induced InSb Nanosails: A Convenient High Mobility Quantum System, Nano Lett. 16 (2016) 825-833.

37 A. Jalil, S. Agathopoulos, N.Z. Khan, S.A. Khan, M. Kiani, K. Khan, L. Zhu, New physical insight in structural and electronic properties of InSb nano-sheet being rolled up into single-wall nanotubes, Appl. Surf. Sci. 487 (2019) 550-557.

38 J. P. Perdew, K. Burke, and M. Ernzerhof, Generalized gradient approximation made simple, Phys. Rev. Lett. **77**, 3865 (1996).

39 J. P. Perdew, K. Burke, and M. Ernzerhof, Generalized gradient approximation made simple, Phys. Rev. Lett. **78**, 1396 (1997).

40 G. Kresse and J. Hafner, Ab initio molecular dynamics for liquid metals, Phys. Rev. B **47**, 558 (1993).

41 G. Kresse and J. Hafner, Efficient iterative schemes for ab initio total-energy calculations using a plane-wave basis set, Phys. Rev. B **49**, 14251 (1994).

42 J. Heyd, G. E. Scuseria, and M. Ernzerhof, Screened hybrid density functionals applied to solids, J. Chem. Phys. **118**, 8207 (2003).

43 H.J. Monkhorst and J.D. Pack, Special points for Brillouin-zone integrations, Phys. Rev. B **13**, 12, (1976).

44 G. Henkelman, A. Arnaldsson, and H. Jonsson, A fast and robust algorithm for Bader decomposition of charge density, Comput. Mater. Sci. **36**, 354 (2006).

45 S. J. Grimme, Semiempirical GGA-type density functional constructed with a long-range dispersion correction, Comput. Chem. **27**, 1787 (2006).

46 D. Alfe, PHON: A program to calculate phonons using the small displacement method, Comput. Phys. Commun. **180**, 2622 (2009).

47 S. Cuenot, C. Fretigny, S. Demoustier-Champagne, and B. Nysten, Surface tension effect on the mechanical properties of nanomaterials measuredby atomic force microscopy, Phys. Rev. B **69**, 165410 (2004).

48 T. Kehoe, J. Bryner, V. Reboud, J. Dual, and C. M. S. Torres, no-scale effects on Young's modulus of nanoimprint polymers measured by photoacoustic metrology, J. Phys. Conf. Ser. **214**, 012049 (2010).

49 W. C. Hu, Y. Liu, D. J. Li, X. Q. Zeng, and C. S. Xu, Comput. Mater. Sci. 83, 27 (2014).